Draft September 30, 2010

Variability and jet motions in BL Lacertae object PKS 1413+135

Frank Ghigo, Yuri Y. Kovalev[†,‡], and Glen Langston

National Radio Astronomy Observatory, P.O. Box 2, Green Bank, WV 24944, U.S.A.

fghigo@nrao.edu; ykovalev@nrao.edu; glangsto@nrao.edu

ABSTRACT

The BL Lac object PKS 1413+135 was observed with the VLBA at several epochs in 2001 at three frequencies (5, 8.4, and 15.4 GHz) to study the compact double lobed radio structure. Significant variation is seen in the core flux on the time scale of a month, but little variation is seen in the jet structure on this scale. No shift in position of the base of the jet with frequency was found. The spectral index maps show an inverted spectrum for the core component and steep spectrum for the jet components. The core spectrum is separated from the total spectrum by subtracting a model determined at lower frequencies. This derived spectrum is in agreement with the measured core fluxes derived from our maps. Fitting of kinematic models to the main jet have been inconclusive.

Subject headings: galaxies: active — galaxies: jets — radio continuum: galaxies — BL Lacertae objects: individual (PKS 1413+135)

1. Introduction

The well-known red BL Lac object PKS 1413+135 (see Perlman et al. 2002 for a review) exhibits much greater variability at higher frequencies ($\nu > 5$ GHz) than at lower frequencies, as seen by the Green Bank Interferometer monitoring program (Lazio et al. 2001). The variability indicates a very compact core, and this and its other unusual properties made it a good candidate for observations with space VLBI. Thus it was included in observations

[†]Jansky fellow, National Radio Astronomy Observatory

[‡]Also at Astro Space Center of Lebedev Physical Institute, Profsoyuznaya 84/32, 117997 Moscow, Russia

with the HALCA space VLBI satellite in 1996 through 1999 (Langston et al. 2000). A preliminary examination of the space VLBI observations suggested there were significant structural changes in the inner part of the western jet on time scales of less than a year. This motivated the VLBI observations reported here, undertaken to look for short term changes in structure, as well as to generally improve the understanding of this object.

PKS 1413+135 was classified as a BL Lac object due to its highly polarized near-IR continuum, line-less optical spectrum and extreme radio variability (Bregman et al. 1981, Beichmann et al. 1981, Stocke et al. 1992, Perlman et al. 1996). It is unique among BL Lacs in having a spiral host (McHardy et al. 1991, Stocke et al. 1992, Perlman et al. 2002). By comparison, "unified" theories for AGN associate BL Lacs with beamed FR 1 radio sources, found in giant elliptical galaxies (Urry & Padovani 1995). VLA observations reveal no kpc-scale structure to a dynamic range of 9600:1 (Perlman & Stocke 1994, Perlman et al. 1994). Under unified schemes this would indicate a highly beamed source, yet at mas scales PKS 1413+135 is clearly two-sided, indicating that it is seen close to the plane of the sky (Perlman et al. 1996). Thus this source presents a severe challenge to unified schemes.

The broadband spectrum of PKS 1413+135 shows a steep cutoff in the near–IR (Beichmann et al. 1981), and a heavily absorbed X-ray spectrum, yielding $N(H) > 2 \times 10^{22}\mathrm{cm}^{-2}$ (Stocke et al. 1992). Redshifted 21 cm observations (Carilli et al. 1992) detected an absorbing column of $N(\mathrm{HI}) = 1.3 \times 10^{19}(T_\mathrm{s}/f)\mathrm{cm}^{-2}$. Time-variable CO (J=1–0), HCO+ (J=2–1, 3–2), and HCN (J=1–2, 2–3) absorption has been detected by Wiklind & Combes (1991, 1994) suggesting that the AGN is behind a Giant Molecular Cloud (GMC) in the optical galaxy. VLBI observations in the redshifted 115 GHz CO line (Conway 1999) show an optical depth on the longest baselines (fringe spacing $\sim 70\mu$as) approximately equal to that obtained with contemporaneous single-dish spectra, indicating the presence of extremely compact structure in the absorbing screen. Interestingly, there is no evidence that the extincted AGN heats the absorbing gas, e.g. bright emission lines from a Narrow Line Region (NRL) or a mid-IR thermal continuum. To explain this dilemma, Perlman et al. (1994) and Stocke et al. (1992) proposed that the AGN is background to the observed galaxy and perhaps gravitationally lensed.

VLBA observations at 8.4 GHz Perlman et al. (1994, 1996) reveal complex two-sided structure. The bend in the Eastern jet is direct evidence for interactions with a dense nuclear medium. At 1.6, 2.3, and 5 GHz (Perlman et al. 1996) a mini-wide-angle-tail structure emerges, spanning ~ 100 mas.

Since the images do not show a second image or arc, they rule out macro-lensing, but not micro-lensing by a GMC in the optical galaxy (e.g., Narayan & Schneider 1990). The images are very similar to those of GPS and CSO such as 0710+439 and 2352+495 (Conway

et al. 1992, Readhead et al. 1994), as noted by Perlman et al. (1994).

There are two possible explanations for these observed properties. One is that it is a very young source (see, e.g., Readhead et al. 1996, O'Dea & Baum 1997). Alternatively, it may be an older source frustrated by interactions with a dense confining medium. Readhead et al. (1994) have dismissed the latter possibility for 2352+495, since a frustrated source would require free-free absorption, which would quench the radio source below a few GHz, and excessive mass requirements within the inner 100 pc ($\sim 2 \times 10^{11} M_{\odot}$). The situation for PKS 1413+135 is similar, although the extreme steepness of the spectrum of the extended structure ($\alpha \sim 2$, Perlman et al. 1996) is tantalizing.

We adopt a Hubble constant $H_0 = 70$ km s^{-1} Mpc^{-1} and a Friedmann–Robertson–Walker cosmology with $\Omega_{\rm m} = 0.3$, $\Omega_{\Lambda} = 0.7$. Thus, with a redshift for PKS 1413+135 of 0.24671 (Carilli et al. 1992) , an angular size of 1 mas corresponds to 3.87 pc, or 12.62 l.y.[1]

This paper presents new observations of PKS 1413+135 and compare the structure at three radio frequencies, 5, 8, and 15 GHz. VLBA observations and data processing are discussed in § 2. Modeling of the source structure is presented in § 3. Components identification and derived apparent speeds are presented in § 4. An analysis of a possible core shift with frequency is made in § 5. Spectral index images of the radiating material as well as total broad-band spectrum of the object are discussed in § 6. A helical jet fit to the structure is made in § 7. We summarize results in § 8.

2. Observations and Data Reduction

Observations were carried out at three frequency bands of 5, 8.4, and 15 GHz during three observing sessions (February 28, April 1, and April 30, 2001) using the 10-element VLBA. We observed using 1 bit samples in right and left circular polarization with a bit rate 128 Mbit/s. Parameters of the observations are summarized in Table 1. During each session, each of the three frequency bands were observed. The observations were organized into several 8 to 9.5 minute scans at each frequency. During the allotted 8 hours of observations, the three frequency bands were observed in alternation. The amplitude calibration source 3C 345 was observed at each frequency. No phase calibration sources were observed, since 1413+135 has a bright compact core. The data were correlated at the NRAO VLBA correlator in Socorro, NM. The correlator output contains 2 s integrations, each band with two IFs, 16 spectral channels per baseband.

[1]Used the cosmology calculator of Wright (2006).

Prior to hybrid imaging, all processing was performed in the NRAO Astronomical Image Processing System (AIPS; Greisen 2003). Sampler bias correction together with initial amplitude calibration was performed using the recorded system temperatures and gain tables (tasks "ACCOR" and "APCAL" through the "VLBACALA" procedure). Prior to fringe fitting, the supplied pulse calibration information was applied (task "PCCOR" through the "VLBAPCOR" procedure). Global fringe fitting was performed with the task FRING (through the "VLBAFRNG" procedure) to remove the remaining delay and rate errors, after choosing a stable, central reference antenna such as Pie Town (PT). A bandpass correction was then determined with the task BPASS. The data were then averaged across the channels within each IF. Editing in a station-based manner, additional flagging, self-calibration, and hybrid imaging was done using Caltech VLBI program DIFMAP (Shepherd, Pearson, & Taylor 1994, Shepherd 1999).

In addition to our three VLBA epochs in 2001, February–April, we have added two additional observations at 15 GHz to include with the analysis of jet motions. 1) VLBA plus phased VLA on 2001, January 4, in the framework of a project (Lister et al. (2003)) for phase calibration of a target source and 2) VLBA data collected in 2001, January 21, for the 2 cm VLBA monitoring project[2] (Kellermann et al. 2004, hereafter K04). Table 2 lists the five epochs of 15 GHz data and indicates the number of antennas in each. Unfortunately no two epochs have exactly the same antenna configuration. Table 2 gives the beam dimensions showing how the resolution differs among the five epochs.

FITS CLEAN images as well as the flagged and calibrated complex visibility function data of the reduced VLBA observations for 1413+134 are available on-line[3].

Cleaned images are displayed in Figure 1 for the three frequencies and three epochs. The peak and total clean fluxes for these maps are shown in Table 2. The lowest contour on all maps in Figure 1 is 0.4 mJy/beam, about three times the rms noise level.

One may readily see that the eastern jet has a somewhat steeper spectrum than the western jet, since it is very prominent at 5 GHz, but hardly detectable at 15 GHz.

[2]http://www.nrao.edu/2cmsurvey/

[3]See electronic edition of the paper in Astrophysical Journal

3. Component fitting

Gaussian components were fit using the Levenberg-Marquardt non-linear least squares minimization technique to the calibrated visibility data in the program DIFMAP. We first fit the core component at the location of the peak flux, subtracted this component, and fit components at the remaining major peaks. These were fit, subtracted, and the process repeated until no significant components were left and the RMS on the residual map was below about 0.4 mJy. The list of fitted parameters is given in Table 3. The fitting of components in this way is not unique. Choices are made in some cases to model a region by two components or by a single extended component. The choices were guided by reference to the appearance of the cleaned maps and by the desire to compare properties at the different epochs and different frequencies. Although the modeling is not unique, many alternative choices of component assignments were tried, and sets of components that fit the data badly become apparent because the model fitting did not converge. Thus the set of model components presented here are believed to be a faithful representation of the data. Any additional components that might be added would have to contain integrated flux densities of about one mJy or less.

Errors in the fitted parameters are estimated based on the discussion by Fomalont (1999). The error in integrated flux density of a component, S, is given by:

$$\Delta S = \sqrt{(S\frac{\Delta R}{P})^2 + \Delta R^2 + (\Delta S)^2_{\rm cal}}\,, \quad (1)$$

where ΔR — root-mean-square (RMS) flux density on the residual map at the component location, P — peak component's intensity, $(\Delta S)_{\rm cal}$ is the the amplitude calibration error. It is equal to about $0.05S$ according to our comparison with the total broad-band spectrum measured quasi-simultaneously with RATAN–600. It agrees with estimations presented by Wrobel & Ulvestad (2006) for a general 1–10 GHz VLBA flux density calibration accuracy.

The error in the component's location, L, is given by:

$$\Delta L = \Delta R\frac{W}{2P}\,, \quad (2)$$

where W is the full width at half maximum (FWHM) of a Gaussian component. This is basically the width divided by signal-to-noise ratio. Since the fitted major axis, W, for some components is very small (i.e., essentially a point) and since W appears in the equations for error in location, this may lead to unreasonably small estimates of position error. We have followed a suggestion based on experience of the 2 cm VLBA survey group (private communication) and used 0.1 mas as the conservative minimum position error at λ 2 cm. Scaling to the other frequencies, we have used 0.2 mas at λ 3.6 cm and 0.3 mas at λ 6 cm.

The minimum detectable angular size ($\theta_{\rm lim}$) was calculated for each component using the following formula derived by Kovalev et al. (2005):

$$\theta_{\rm lim} = b_\psi \sqrt{\frac{4\ln 2}{\pi} \ln\left(\frac{\rm SNR}{\rm SNR - 1}\right)}. \quad (3)$$

where b_ψ is the half-power beam size measured along position angle ψ, and SNR $= \frac{P}{\Delta R}$. For the Gaussian components, we have calculated θ_{lim} for the position angles of the major and minor axes of the fitted component. If the major or minor axis is less than θ_{lim} then the value of θ_{lim} is given as an upper limit to the size in Table 3.

The model fitting results are given in Table 3. Component designations are illustrated in Figure 2a, b, c, and d. Components were designated 'A', 'B', and so forth, starting at the east, and progressing to "H" at the west end; the exception is the core component, designated "K". The zoomed view of Figure 2d shows components D1 and D2, which do not appear as distinct components in the contour maps, but are required to account for all the flux in the modelling of the visibility data. Apparently D1 and D2 represent a ridge of emission joining the core with the outer components. Components 'A', 'B', and 'C' are the same as named by Perlman et al (1996). The western jet, called 'D' by Perlman et al.(1996), consists of several components, which we call 'D1', 'D2', 'E1', 'E2', 'F1', 'F2', 'G', and 'H'.

In the counter-jet, component 'A' appears at 5 GHz as two parts which we call 'A1' ($\Delta\alpha \approx 33$ mas) and 'A2' ($\Delta\alpha \approx 27$ mas). But at 8.4 GHz, 'A2' does not appear, probably because it is more diffuse than 'A1'. Neither part of 'A' is seen at 15.4 GHz. Component 'B' ($\Delta\alpha \approx 17$ mas) has consistent properties at for all epochs and frequencies. It is clearly double, as seen on the 8.4 GHz map, but we have modeled it as a single elliptical Gaussian.

In the region of component 'C', a single component ('C2') is seen at 15.4 GHz, two ('C1', 'C2') at 5 GHz, and three ('C1', 'C2', 'C3') are seen at 8.4 GHz.

4. Component Motions

Radial motions in the western jet were estimated by comparing the positions of components at the five epochs of 15.4 GHz observations (see Table 2). We have compared our data with kinematic results from the 15 GHz monitoring program (K04). In that paper, three components in the western jet are designated 'B', 'C', and 'F', lying about 2.5, 4.5, and 7.5 mas from the core, respectively. These appear to correspond to components which we call 'E2', 'F1', and 'G', respectively.

The point component fit at the peak in the map is referred to as the "core". The location

of the core is in all cases only a few hundredths of a milliarcsecond from the mapping phase center position. The location of the core was subtracted from the location of each of the other components; thus all component locations are given relative to the core. The identification of the three components which we call 'E2', 'F1', and 'G' is shown in Figure 3.

The radial offsets from the core of the three components at the five epochs are plotted in Figure 4. Linear fits of location versus time were done for each component, and the results are listed in Table 4. One can see that the speeds of the components in the western jet are consistent with zero motion, i.e., we cannot detect any motion of these components over the four-month span of these observations.

The positions of the three components 'E2', 'F1', and 'G' were compared with the data presented by K04 which showed component positions observed over a six year span having speeds of 0.25 mas yr^{-1} for 'E2' (their 'B'), 0.37 mas yr^{-1} for 'F1' (their 'C'), and 0.45 mas yr^{-1} for 'G' (their 'F'). In Figure 4 we show dashed lines indicating the position of components 'E2' and 'G' predicted by K04, based on the speed and zero point. They did not give a zero point for component 'F' because the fit was of poor quality. One can see (Table 4) that our results are consistent with those of K04 within the quoted errors.

5. Core shift analysis

The core component is most likely not at the position of the presumed black hole, but at the base of the jet, whose position may vary with frequency due to optical depth effects (see, e.g., Lobanov 1998). This effect has been sought in the present data by matching components 'E2', 'F1', and 'G' as fit to the 15 GHz data with the nearest components fit at the other two frequencies. These are the only components in the western jet that have counterparts at all three frequencies.

The offsets from the core as a function of frequency are plotted in Figure 5. The solid lines show linear least squares fits for each component, and fit parameters are listed in Table 5. The data show a significant shift with frequency for component 'E2'.

If we were seeing a shift of the core position, then we would expect that all components would have the same position shift with frequency. But a significant shift is seen only in component 'E2', thus we cannot be seeing a shift of the core, but only an effect of optical depth at that component. Thus we can place an upper limit on the core shift of three times the average one-sigma error, or about 0.045 mas GHz^{-1} in the frequency range 5–15 GHz.

6. Spectral analysis

6.1. Spectral index images

We have constructed the two-frequency spectral index images for 5–8 and 8–15 GHz intervals (see Figure 6). As expected, the core region appears to be optically thick with optically thin jet features. A spectral aging is observed for the jet with spectral index α changing from -0.5 to -2 which corresponds to the evolution of the distribution of electrons energy with power γ from 2 to 5 assuming a power law $N(E) = N_0 E^{-\gamma}$.

6.2. Component 'C2'

An unusual spectral index gradient is observed at 5–8 GHz in the eastern jet component 'C2' (see zoomed 'C2' component spectral index imaged in Figure 7). This happens at all three of our multi-epoch experiments and exhibits itself also in a shift of the component's centroid between 5 and 8 GHz. This effect could result from absorption by the same material as detected in HI line observations by Perlman et al. (2002) in the central region of PKS 1413+135. While intriguing, this centroid shift of about 0.3 mas is of the same order as the formal error in the component position. More observing would be required to confirm this phenomenon.

6.3. Total broad-band spectrum

Kovalev et al. (1999, 2002) suggested that the total broad-band spectrum of almost all AGNs could be modeled by a sum of two components: a slowly variable optically thin one dominating at low frequencies, and a compact variable one dominating at high frequencies.

We have incorporated data from the literature (Ulvestad et al. 1981, Perley 1982, Wright & Otrupcek 1990, Douglas et al. 1999, White et al. 1997, Condon et al. 1998) at frequencies below 1.4 GHz to model with high accuracy the low frequency slowly variable part of the spectrum. The use of heterogeneous measurements made at different epochs is defensible by the confirmed assumption of slow variability in this spectral region. These data are plotted in Figure 8 as black filled circles; the long-dash line shows the fitted optically thin spectrum with $\alpha = -0.64$, which gives an estimation of the power law index of the energy distribution of the emitting particles as $\gamma = 2.28$.

Higher frequency points come from this paper and from RATAN-600 measurements.

The blue squares and blue dotted line in Figure 8 show the total cleaned flux in the maps at 5.0, 8.4, and 15.4 GHz observed on April 1, 2001, as listed in Table 2. The RATAN-600 measurements, made March 28, 2001, are shown as red squares with 1σ error bars. If one subtracts the fitted optically thin spectrum (long-dash line) from the RATAN data, one obtains the spectrum of the variable compact component, plotted as filled red triangles and short-dash line.

This derived spectrum of a compact component may be compared with the flux density of such a component as estimated by the peak flux in each map (see Table 2), and plotted as blue triangles in Figure 8. One may see that these estimates are in reasonable agreement with the derived compact spectrum; thus the accuracy of this spectral decomposition is confirmed.

The derived spectrum of this compact rapidly variable structure appears optically thick with $\alpha = +1.6$ between 2 and 5 GHz. This value is much lower than predicted ($\alpha = +2.5$) from the canonical spectrum of an homogeneous synchrotron source. We conclude that the compact rapidly variable feature of the object is significantly more complex than a homogeneous case (geometrical shape and/or magnetic field distribution).

7. Jet helical structure

.

The bends in the jet of PKS 1413+135 suggest a helical structure. We have attempted to fit kinematic helical jet models as described by Steffen et al. (1995) to match the form of the ridge of emission of the western jet (which we believe is beamed towards us).

7.1. Ridge Line

The observed emission ridge was derived from the 15 GHz map of January 4, 2001, which was the one with the highest resolution and best signal-to-noise. The ridge line was estimated by adopting a polar coordinate system centered on the core. For sucessive values of the radial coordinate, an average over all azimuths, weighted by the flux density, gives the ridge line point. The method was adapted from an algorithm by Matt Lister (private communication). The derived ridge line is shown superimposed on the map in Figure 9.

7.2. Numerical Simulations

Models were fit based on "model 3" of Steffen et al. (1995). In these models regions of emission follow a helical path on the surface of a cone of opening half-angle ψ. The axis of the cone is inclined to the line of sight by an angle θ. The emission blob starts at an initial radius of r_0 with a speed of β, and an angular speed ω_0.

Thousands of simulations were run over a wide range of possible parameter space. Constraints on the parameters β and θ are imposed by measurement of the apparent speed (β_{app}) of a relativisitically moving object:

$$\beta_{app} = \frac{\beta sin\theta}{1 - \beta cos\theta}$$

We have used the measurement of the apparent speed of component E2 by Kellermann et al. (2004), which they refer to as component "B". The reliability and accuracy of the determination of its apparent speed is listed as "excellent" by Kellermann et al. (2004). Using their value of (3.9±1.2)c, the above equation leads to the constraints

$$\beta > 0.94c \;\; and \;\; \theta < 40\,\mathrm{deg}$$

Despite running many simulations, no clear optimum model was found. The many parameters allowed many possible models that fit the ridge line reasonably well. We found that by trying to minimize the Chi-square deviation between the observed and predicted ridge lines, we were led to solutions with lower values of β than given by the above constraint. Thus we have an apparent contradiction between the minimum intrinsic component speed implied by the measured apparent speed and the lower speeds required by the better fitting models.

We show one of the best fitting models in Figure 9; the parameters are listed in Table 6. The solid curve shows the model, and the dotted lines the measured ridge line. The model has tight spiral loops near the core which become larger both in amplitude and length as they move further from the core. These are not seen in our maps, but if one convolves the model curve with the beam, the apparent straightness of the jet in the inner 3 mas is consistent with the model.

8. Summary

Five epochs of VLBI observations of PKS 1413+135 at 3 frequency bands are presented. These observations show the jet structure is changing slowly during this time, despite the very rapid changes in core brightness at 15 GHz. We have computed spectral index maps and fit the structure of the jet to the model of Steffen et al. (1995).

The total broad-band spectrum is shown to be reasonably well modeled as a steep-spectrum synchrotron component and a compact optically thick variable component.

The National Radio Astronomy Observatory is a facility of the National Science Foundation operated under cooperative agreement by Associated Universities, Inc. We thank the VLBA staff for their dedication to providing high quality VLBI facilities. RATAN–600 observations were partly supported by the Russian State Program "Astronomy" and the Russian Ministry of Education and Science, the NASA JURRISS Program (project W–19611), and the Russian Foundation for Basic Research (projects 01–02–16812 and 05–02–17377). We have used VLBA calibrated visibility function data for PKS 1413+135 from the 2 cm VLBA monitoring program (e.g., K04) to supplement our observations during the beginning of 2001 The authors made use of the database CATS (Verkhodanov et al. 1997) of the Special Astrophysical Observatory. This research has made use of the NASA/IPAC Extragalactic Database (NED) which is operated by the Jet Propulsion Laboratory, California Institute of Technology, under contract with the National Aeronautics and Space Administration.

REFERENCES

Aller, Margo F., Aller, Hugh D., Hughes, Philip A. & Latimer, George, 1999, ApJ, 512, 601

Beichmann, C., Neugebauer, G., Soifer, B., Wooten, G., Roellig, T., & Harvey, P. 1981, Nature, 293, 711

Bregman, J., Glassgold, A., Huggins, P., & Kinney, A. 1981, Nature, 293, 714.

Carilli, C. L., Perlman, E. S., & Stocke, J. T. 1992, ApJ, 400, L13

Condon, J. J., Cotton, W. D., Greisen, E. W., Yin, Q. F., Perley, R. A., Taylor, G. B., & Broderick, J. J. 1998, AJ, 115, 1693

Conway, J. E. & Murphy, D. W. 1993, ApJ, 411, 89.

Conway, J. E., 1999, New Astronomy Reviews, 43, 509.

Conway, J. E., Pearson, T. J., & Readhead, A. C. S. 1992, ApJ, 396, 62

Darling, Jeremy 2004, ApJ, 612, 58.

Douglas, J. N., Bash, F. N., Bozyan, F. A., Torrence, G. W., & Wolfe, C. 1996, AJ, 111, 1945

Fomalont, E. B. 1999. "Synthesis Imaging in Radio Astronomy", Taylor, Carilli, Perley, eds. ASP Conference Series 180, p301.

Greisen, E. W. 2003, in Astrophysics and Space Science Library 285, Information Handling in Astronomy – Historical Vistas, ed. A. Heck (Dordrecht: Kluwer), 109

Kellermann, K. I., & Pauliny-Toth, I. I. K. 1969, ApJ, 155, L31

Kellermann, K. I., Lister, M. L., Homan, D. C., Vermeulen, R. C., Cohen, M. H., Ros, E., Kadler, M., Zensus, J. A., & Kovalev, Y. Y. 2004, ApJ, 609, 539 (K04)

Kovalev, Yu. A. 1998, Bull. SAO, 44, 50

Kovalev, Y. Y., Nizhelsky, N. A., Kovalev, Y. A., Berlin, A. B., Zhekanis, G. V., Mingaliev, M. G., & Bogdantsov, A. V. 1999, A&AS, 139, 545

Kovalev, Y. Y., Kovalev, Yu. A., Nizhelsky, N. A., & Bogdantsov, A. V. 2002, PASA, 19, 83

Kovalev, Y. Y., Kellermann, K. I., Lister, M. L., Homan, D. C., Vermeulen, R. C., Cohen, M. H., Ros, E., Kadler, M., Lobanov, A. P., Zensus, J. A., Kardashev, N. S., Gurvits, L. I., Aller, M. F., Aller, H. D. 2005, AJ, 130, 2473.

Langston, G., Minter, A. H., Ghigo, F., 2000, Adv. Space Res. Vol. 26, p. 701.

Lazio, T. J. W., Waltman, E. B., Ghigo, F. D., Fiedler, R. L., Foster, R. S., Johnston, K. J., 2001, ApJS, 136, 265.

Lobanov, A. P. 1998, A&A, 330, 79

Lister, M. L., Kellermann, K. I., Vermeulen, R. C., Cohen, M. H., Zensus, J. A., & Ros, E. 2003, ApJ, 584, 135

McHardy, I. M., Abraham, R. G., Crawford, C. S., Ulrich, M.–H., Mock A. C., & Vanderspeck, R. K. 1991, MNRAS, 249, 742

McHardy, I. M., Merrifield, M. R., Abraham, R. G., & Crawford, C. S. 1994, MNRAS, 268, 681

Narayan, R., & Schneider, P. 1990, MNRAS, 243, 192

O'Dea, C. P., Baum, S. A., & Stanghellini, C. 1991, ApJ, 380, 66

O'Dea, C. P., & Baum, S. A. 1997, AJ, 113, 1480

O'Dea, C. P. 1998, PASP, 110, 493

Perley, R. A. 1982, AJ, 87, 859

Perlman, E. S., & Stocke, J. T. 1994, AJ, 108, 56

Perlman, E. S., Stocke, J. T., Shaffer, D. B., Carilli, C., & Ma, C. 1994, ApJ, 424, 69

Perlman, E. S., Carilli, C. L., Stocke, J. T., & Conway, J., 1996, AJ, 111, 1839

Perlman, E. S., Stocke, J. T., Carilli, C. L., Sugiho, M., Madejski, G, Wang, Q. D., Conway, J. 2002, AJ, 124, 2401.

Readhead, A. C. S., Xu, W., Pearson, T. J., Wilkinson, P. N., & Polatidis, A. 1994, in Compact Extragalactic Radio Sources, ed. J. A. Zensus, & K. I. Kellermann (Green Bank: NRAO), 17

Readhead, A. C. S., et al. 1996, ApJ, 460, 612.

Shepherd, M. C. 1997, in ASP Conf. Ser. 125, Astronomical Data Analysis Software and Systems VI, ed. G. Hunt, H. E. Payne (San Francisco: ASP), 77

Shepherd, M. C., Pearson, T.J., & Taylor, G. B. 1994, BAAS, 26, 987

Steffen, W., Zensus, J.A., Krichbaum, T.P., Witzel, A., & Qian, S.J. 1995, A&A, 302, 335

Stevens, J. A., et al. 1994, ApJ437, 91.

Stocke, J. T., Wurtz, R., Wang, Q. D., Jannuzi, B., & Elston, R. 1992, ApJ, 400, 17

Ulvestad, J., Johnston, K., Perley, R., & Fomalont, E. 1981, AJ, 86, 1010

Urry, M., & Padovani, P. 1995, PASP, 107, 803

Verkhodanov, O. V., Trushkin, S. A., Andernach, H., & Chernenkov, V. N. 1997, in ASP Conf. Ser. 125, Astronomical Data Analysis Software and Systems VI, ed. by G. Hunt, & H. E. Payne (San Francisco: ASP), 322

White, R. L., Becker, R. H., Helfand, D. J., & Gregg, M. D. 1997, ApJ, 475, 479

Wiklind, T., & Combes, F. 1991, A&A, 328, 42

Wiklind, T., & Combes, F. 1994, A&A, 286, L9

Wilson, A., & Colbert, E. 1995, ApJ, 438, 62

Wright, A., & Otrupcek, R. 1990, PKS90.C, 0000W

Wright, E. L., 2006, PASP, 118, 1711

Wrobel, J. M. & Ulvestad, J. S. 2006, VLBA Status Summary, NRAO; http://www.vlba.nrao.edu/astro/obstatus/current/obssum.html

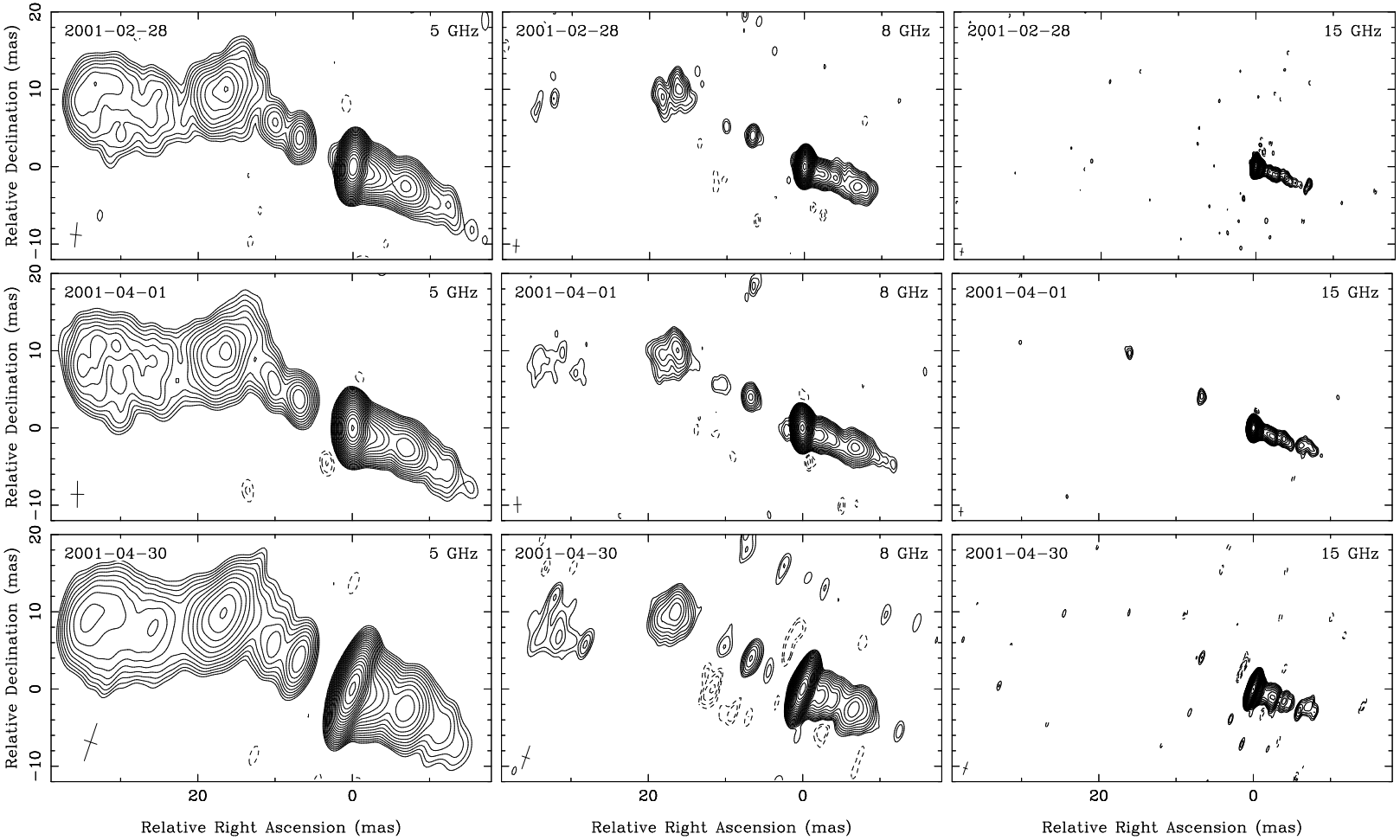

Fig. 1.— VLBA images of PKS 1413+135. The lowest contour is ± 0.4 mJy/beam, increasing by $\sqrt{2}$. See Table 2 for peaks and total fluxes. The UV and image FITS files are available on the web at ...

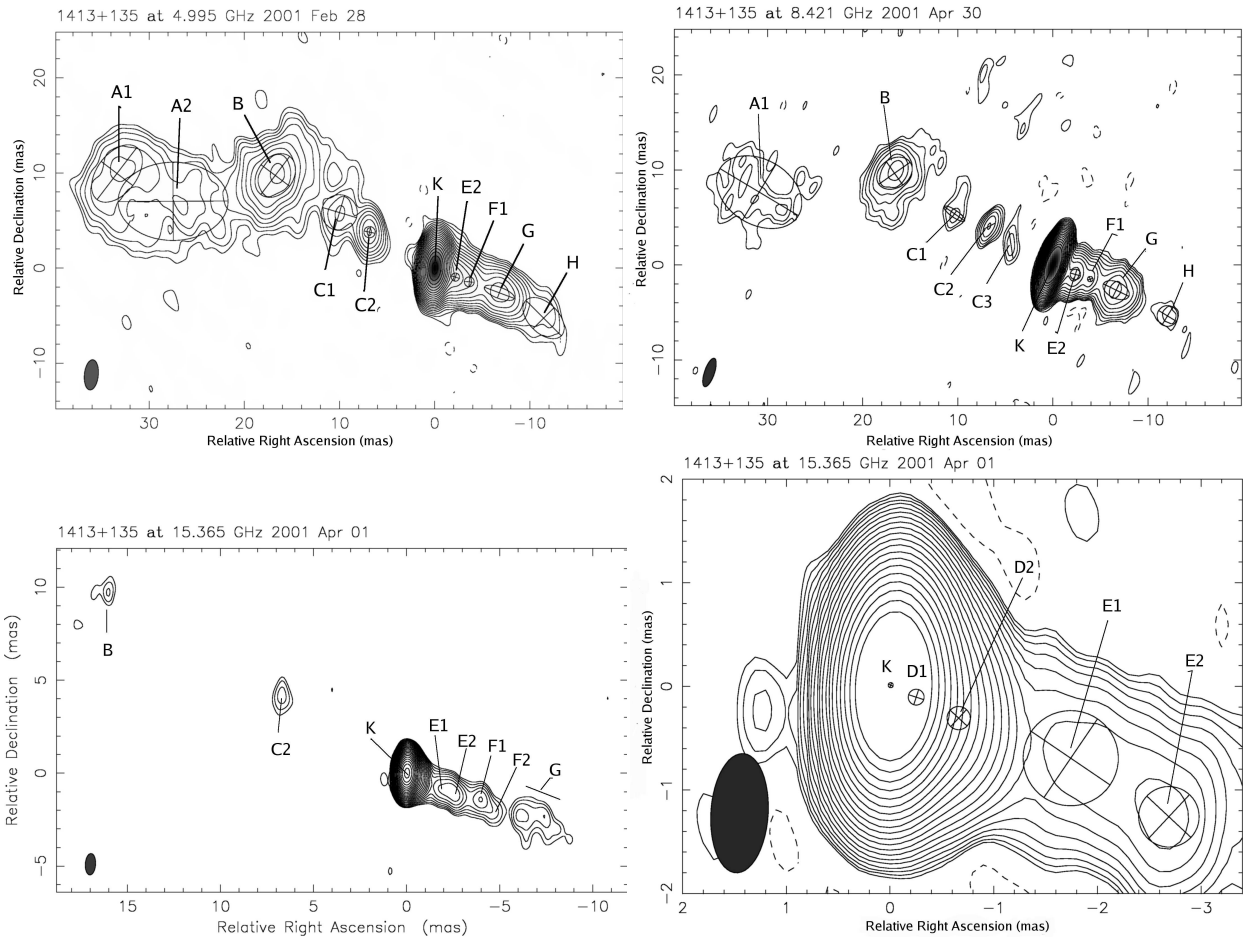

Fig. 2.— Component designations "A", "B", to "H" are indicated. "K" indicates the core component. a)5 GHz map, b)8.4 GHz map, c)15.4 GHz map, d)15.4 GHz map zoomed to show the core region. The clean beam size is shown at lower left of each map. The superimposed ellipses show the component sizes.

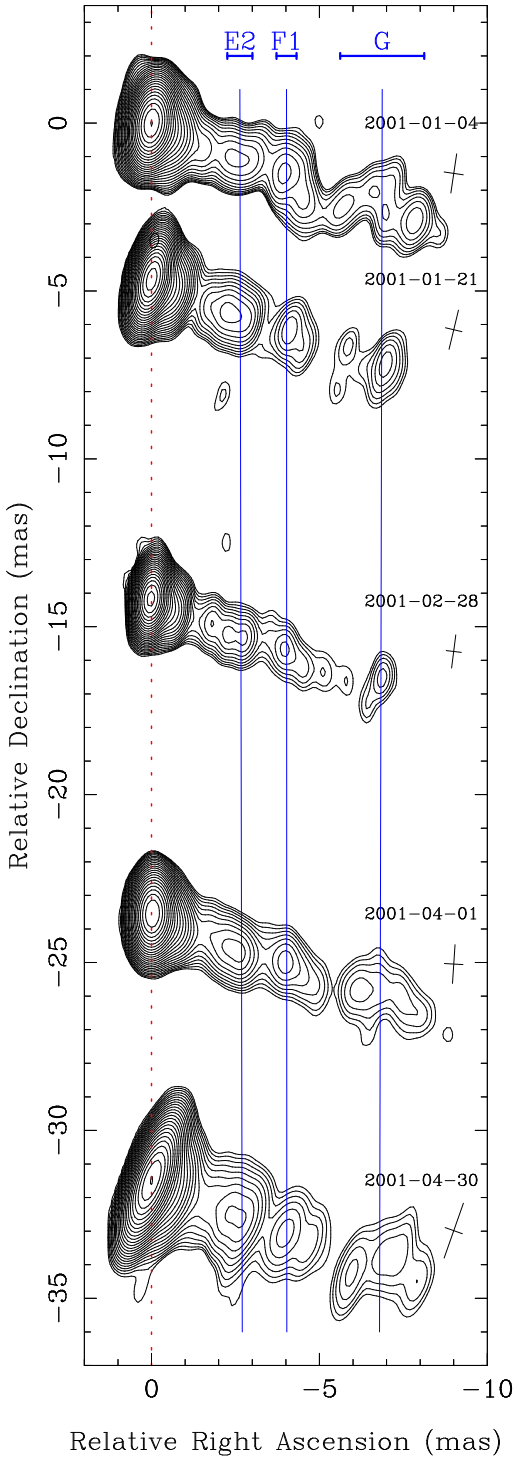

Fig. 3.— The jet evolution at 15 GHz. Five epochs are shown, from top to bottom. The HPBW of the clean beam for each map is shown on the right. Image parameters are presented in Table 2. Lines represent interpolated motion of modeled jet components. Map shift in relative declination is proportional to the time shift (approximately two mas per week or 100 mas per year.).

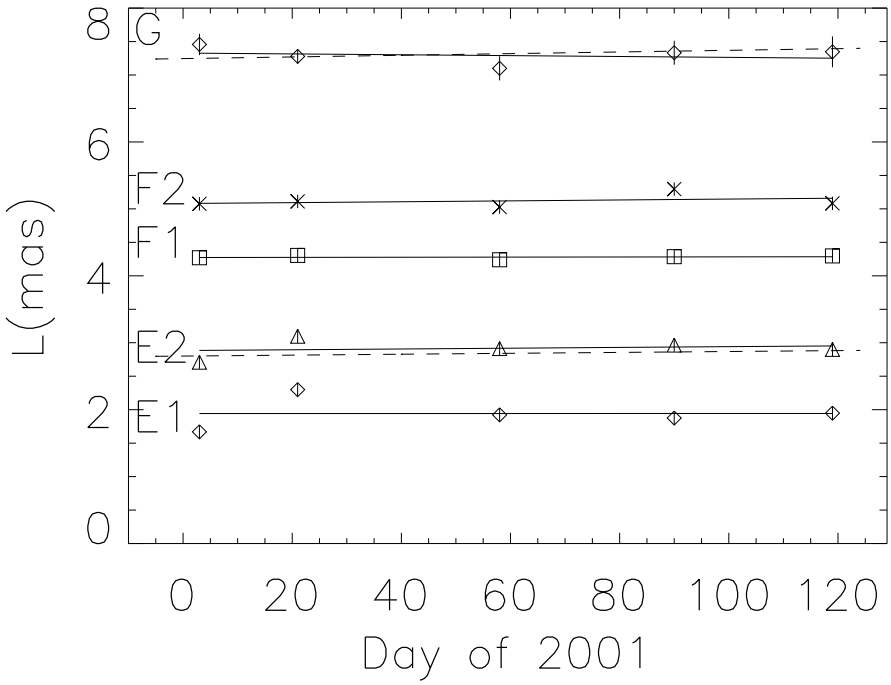

Fig. 4.— Positions as function of time for components 'E1', 'E2', 'F1', 'F2', and 'G'. Solid lines are linear fits to the data points for each component. The horizontal dashed lines show the positions predicted by Kellermann et al. (2004). Refer to Table 4 for the derived speeds.

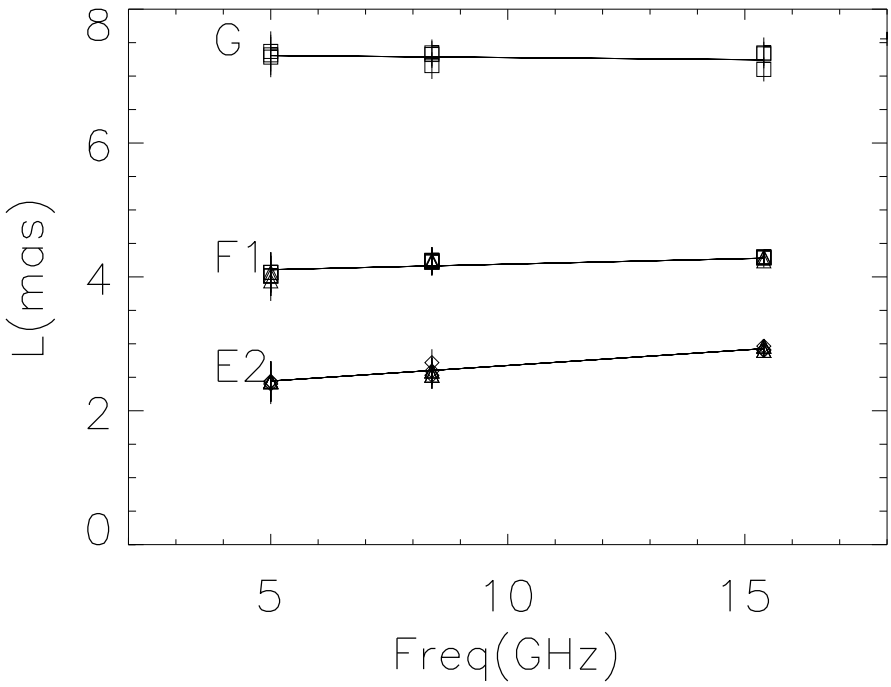

Fig. 5.— Offsets from core at three frequencies. Data from all three epochs are plotted. The solid lines are linear least squares fits. Refer to Table 5 for the fit parameters.

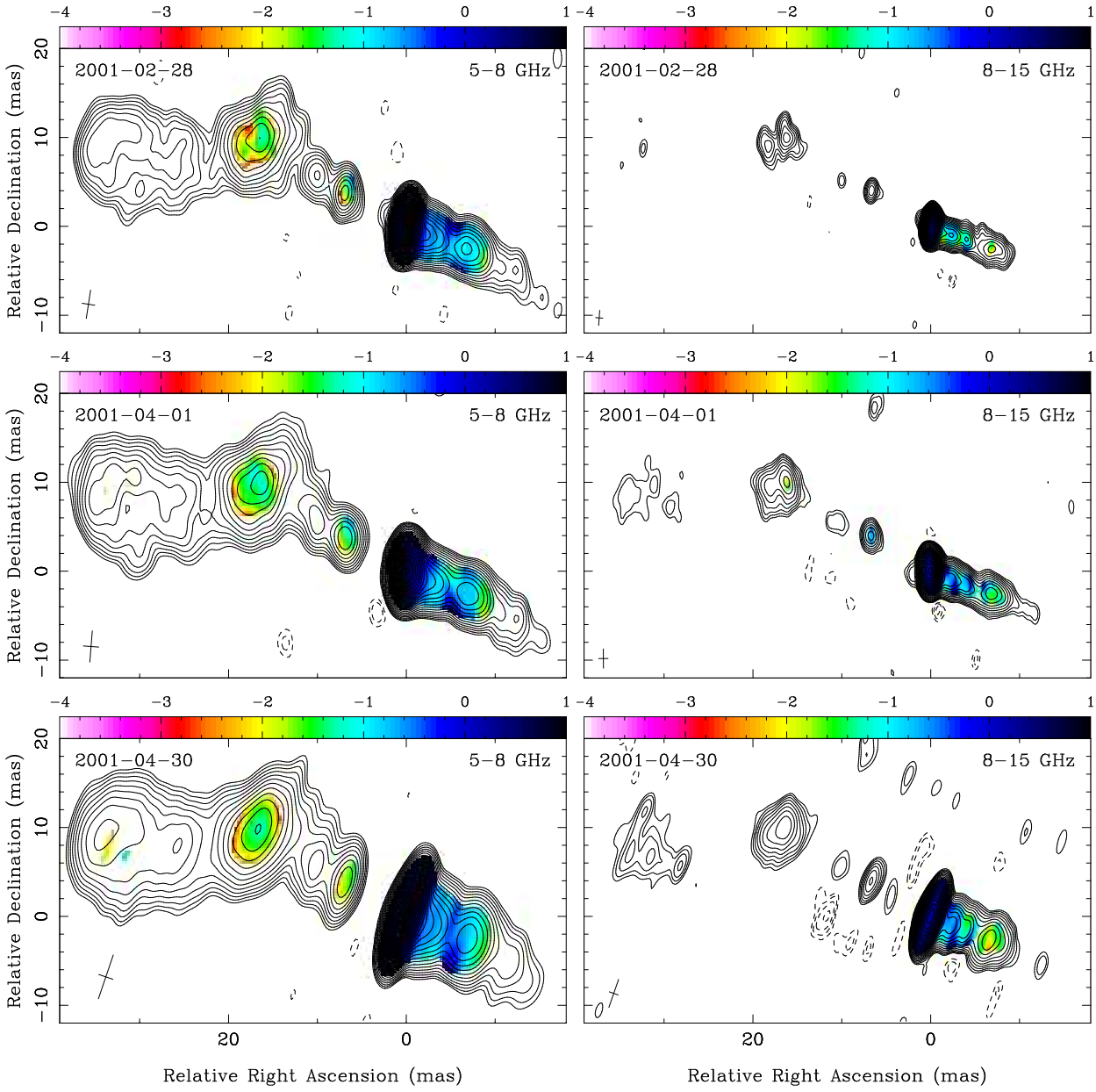

Fig. 6.— Spectral index maps of PKS 1413+135. Color represents spectral index values α ($S \sim \nu^{\alpha}$), contour maps are the lower frequency naturally waited CLEAN images (see parameters in Table 2).

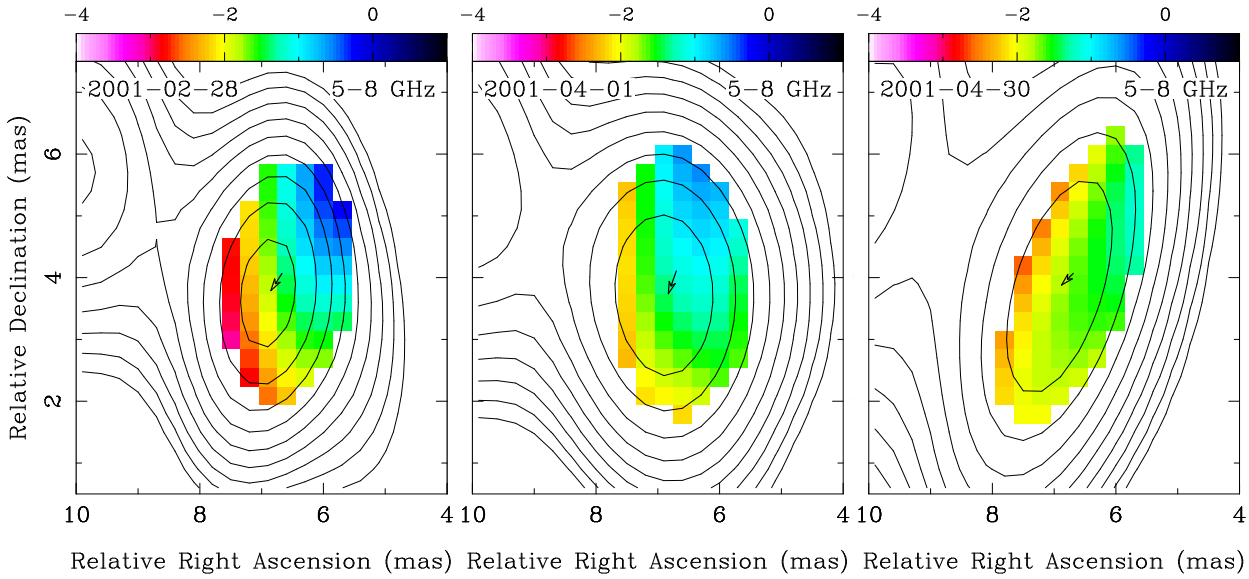

Fig. 7.— Spectral index maps of component C2 (zoomed from Figure 6). The arrows show the shift of the component's centroid location from 8 to 5 GHz according to our modeling results (see Table 3).

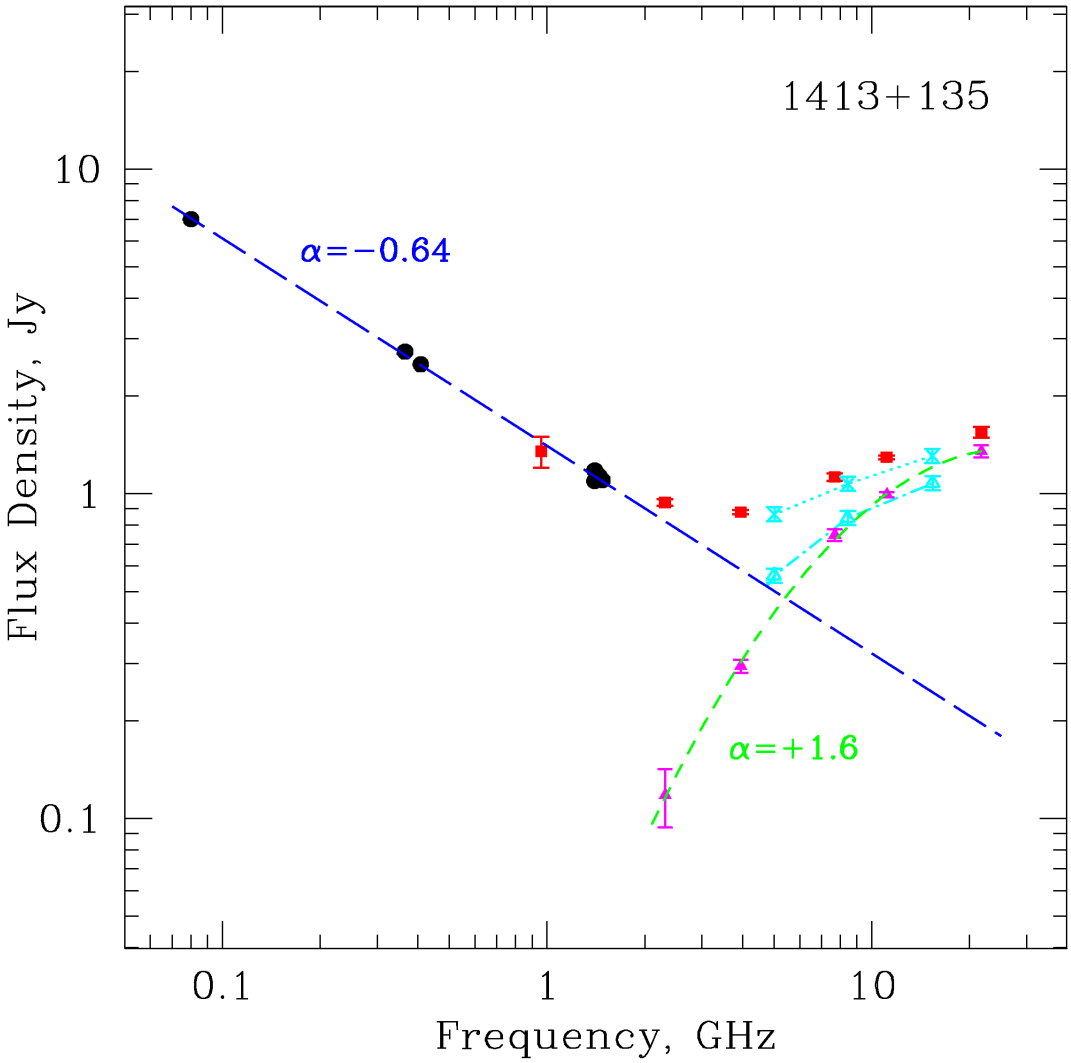

Fig. 8.— Broad-band spectrum of PKS 1413+135. RATAN–600 measurements are marked as red squares, with 1σ error bars; low frequency data from the literature measured at other epochs are black circles. A synchrotron spectrum ($\alpha = -0.64$) fitted to the data at $\nu < 1.5$ GHz is shown as a long-dashed line. Subtraction of this spectrum from the data gives a spectrum of the compact variable component of the source (filled triangles and fitted short-dash line) with spectral index $\alpha = +1.6$. Blue crosses and dotted line represent total CLEAN VLBA flux density of our maps on the epoch April 1, 2001. Blue triangles show the peak flux densities in the maps, an estimate of the compact component.

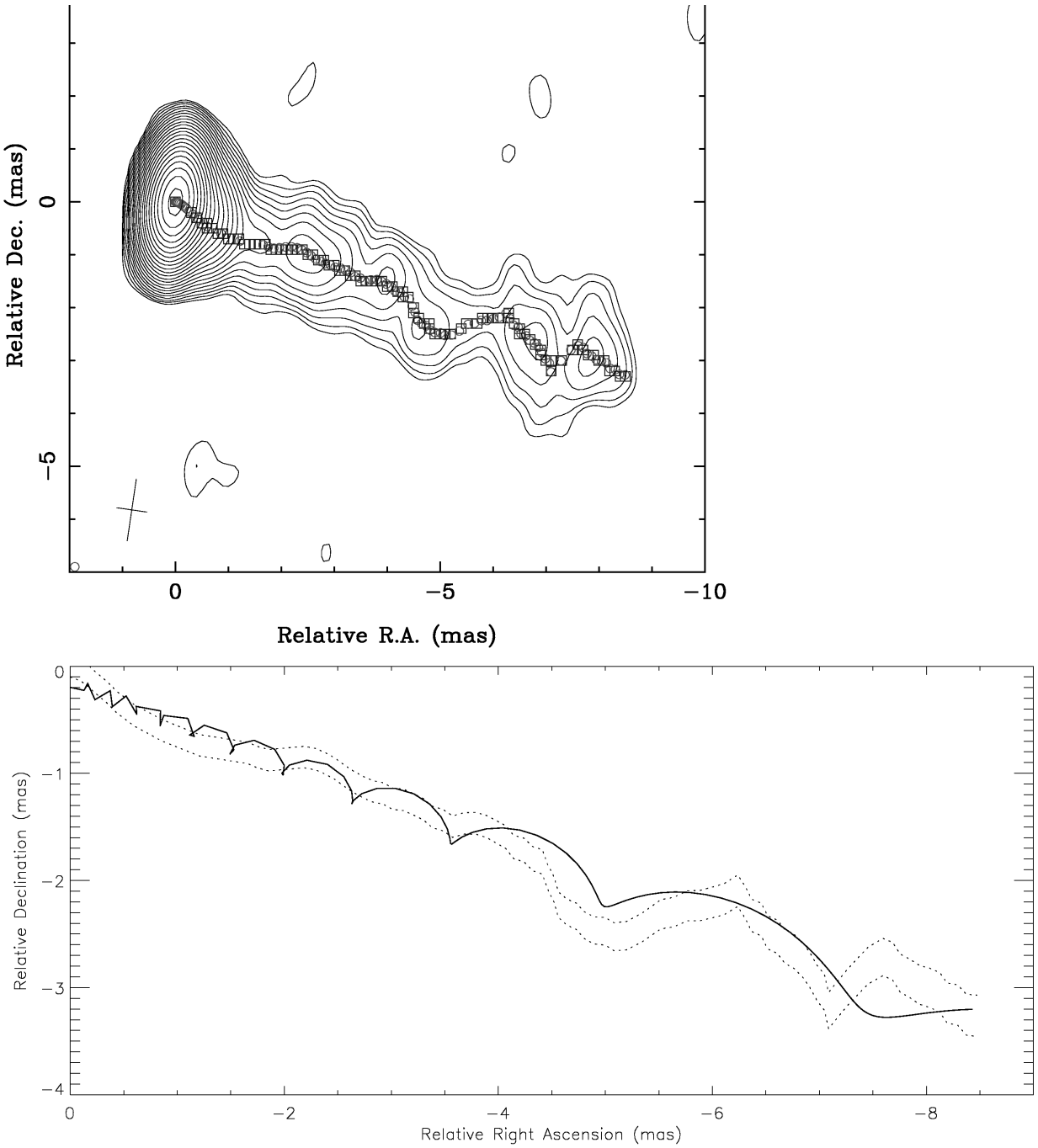

Fig. 9.— A(Upper): Ridge line derived from the 15 GHz image of 4 January 2001. The 1.2x0.6mas beam size is shown at the lower left. B(lower): The helical jet model (solid curve) compared with the derived ridgeline (dotted lines). The two dotted lines show ± one sigma around the derived ridge line. The ridgeline sigma is taken to be the position errors of the fitted components, $\pm 0.10 mas$ within 4 mas of the core, increasing to $\pm 0.16 mas$ at the end.

Table 1. Observational parameters

Frequency, MHz	Total bandwidth, MHz	Integration Time, min
15361.5, 15369.5	16	150
8417.5, 8425.5	16	125
4991.5, 4999.5	16	150

Note. — Quasi-simultaneous three-band VLBA measurements on Feb 28, Apr 01, and Apr 30 were done in both left and right circular polarization. Total bit-rate for each band: 128 Mbps.

Table 2. Parameters of the maps in Figures 1 and 2

Epoch in 2001 (1)	Frequency (GHz) (2)	Antennas (3)	Beam (4)	Peak flux (Jy/beam) (5)	Total flux (Jy) (6)	Ref (7)
Jan 04	15.4	9 + phased VLA[a]	1.17×0.57 at −8°	1.179	1.434	L03
Jan 22	15.4	10	1.20×0.50 at −14°	1.453	1.599	K04
Feb 28	5.0	9[b]	3.19×1.48 at −6°	0.579	0.828	
	8.4		1.76×0.85 at −4°	0.948	1.112	
	15.4		0.99×0.45 at −7°	1.339	1.489	
Apr 01	5.0	9[c]	3.41×1.68 at −1°	0.598	0.863	
	8.4		2.07×1.01 at 2°	0.916	1.071	
	15.4		1.15×0.55 at −4°	1.154	1.306	
Apr 30	5.0	9[d]	5.12×1.72 at −19°	0.634	0.891	
	8.4		3.15×1.05 at −19°	1.006	1.160	
	15.4		1.73×0.54 at −19°	1.184	1.327	

Note. — Col. (1): epoch of observation. Col. (2): central frequency (GHz). Col. (3): number of VLBA antennas. Col. (4): beam parameters: major and minor HPBW (mas), P.A. of the major axis (degrees). Col. (5): peak flux density of a CLEAN naturally weighted image (Jy/beam). Col. (6): integrated flux density of a CLEAN naturally weighted image calculated as a sum of CLEAN compnents (Jy). Col. (7): Data reference if different from this paper: L03: Lister et al. (2003), K04: Kellermann et al. (2004). The lowest contour on all maps is ±0.4 mJy/beam, except for the Jan 04 map for which it is ±0.2 mJy/beam. The interval between contours in Figure 1 is a factor of $\sqrt{2}$, up to the peak value listed in this table.

[a]NL not used.

[b]OV not used, recorder problems.

[c]HN not used, snow/ice on the antenna.

[d]SC not used, data lost.

Table 3. Fitted parameters of components.

Component (1)	Band (2)	Epoch (3)	Flux Density (4)	$\Delta\alpha, \Delta\delta, (\sigma_p)$ (5)	Major(mas) (6)	Minor (7)	PA (8)
K (core)	15.4	Jan 04	1166.6 ± 58.3	···	0.08	···	···
		Jan 22	1439.5 ± 72.0	···	0.06	···	···
		Feb 28	1328.1 ± 66.4	···	0.05	···	···
		Apr 01	1076.8 ± 53.8	···	0.05	···	···
		Apr 30	1098.1 ± 54.9	···	< 0.04	···	···
	8.4	Feb 28	944.9 ± 47.3	···	0.14	···	···
		Apr 01	839.8 ± 42.0	···	< 0.02	···	···
		Apr 30	949.7 ± 47.5	···	0.09	···	···
	5.0	Feb 28	544.0 ± 27.2	···	0.11	···	···
		Apr 01	558.1 ± 27.9	···	< 0.05	···	···
		Apr 30	602.3 ± 30.1	···	0.21	···	···
A1	8.4	Feb 28	18.2 ± 4.1	31.75 8.85 (± 1.04)	9.50	6.23	68
		Apr 01	18.6 ± 3.5	31.01 8.56 (± 0.91)	10.06	6.64	76
		Apr 30	24.4 ± 5.2	30.90 7.64 (± 1.00)	9.61	6.86	59
	5.0	Feb 28	27.8 ± 2.9	33.33 9.95 (± 0.31)	6.90	4.22	−38
		Apr 01	32.6 ± 4.1	33.78 9.32 (± 0.43)	7.48	4.30	−20
		Apr 30	30.6 ± 2.3	33.49 9.77 (± 0.30)	6.82	4.53	−37
A2	5.0	Feb 28	53.3 ± 7.1	27.44 6.98 (± 0.72)	11.63	8.21	−89
		Apr 01	50.4 ± 11.1	26.97 7.22 (± 1.06)	9.91	8.56	51
		Apr 30	51.0 ± 4.8	26.97 7.25 (± 0.44)	11.17	7.76	−75
B	15.4	Jan 04	13.7 ± 2.9	16.71 9.87 (± 0.54)	5.19	3.75	83
		Jan 22	3.8 ± 1.3	16.28 9.96 (± 1.09)	6.41	< 0.41	34
		Feb 28	16.3 ± 4.5	17.81 9.60 (± 1.00)	7.40	4.10	42
		Apr 01	8.7 ± 1.9	16.69 9.65 (± 0.38)	3.62	3.16	−51
		Apr 30	9.6 ± 2.8	16.88 9.96 (± 0.88)	6.15	3.92	73
	8.4	Feb 28	25.1 ± 2.9	16.72 9.74 (± 0.21)	4.18	2.92	−53
		Apr 01	29.5 ± 2.8	16.83 9.63 (± 0.20)	4.36	3.39	−36
		Apr 30	28.4 ± 2.1	16.66 9.65 (± 0.20)	4.02	3.04	−54
	5.0	Feb 28	61.6 ± 3.9	16.74 9.73 (± 0.30)	5.02	3.83	−37
		Apr 01	68.0 ± 4.7	16.79 9.64 (± 0.30)	5.43	4.21	−37
		Apr 30	61.4 ± 3.3	16.77 9.67 (± 0.30)	5.15	3.72	−38
C1	8.4	Feb 28	2.6 ± 0.4	10.22 5.10 (± 0.20)	2.01	1.30	−39
		Apr 01	3.9 ± 0.4	10.66 5.40 (± 0.20)	2.10	1.59	28
		Apr 30	3.6 ± 0.6	10.35 5.38 (± 0.20)	2.66	< 0.90	54
	5.0	Feb 28	10.8 ± 1.1	9.96 5.90 (± 0.30)	4.78	2.84	−22
		Apr 01	10.8 ± 1.1	10.13 6.04 (± 0.30)	4.91	2.54	−15
		Apr 30	13.7 ± 1.0	10.15 6.22 (± 0.30)	5.62	3.93	15
C2	15.4	Jan 04	8.6 ± 2.2	7.22 4.02 (± 0.58)	4.64	2.00	59
		Jan 22	2.9 ± 0.8	7.01 4.32 (± 0.13)	1.17	< 0.30	−56
		Feb 28	3.3 ± 0.9	6.89 4.00 (± 0.18)	1.36	0.93	69

Table 3—Continued

Component (1)	Band (2)	Epoch (3)	Flux Density (4)	$\Delta\alpha, \Delta\delta, (\sigma_p)$ (5)	Major(mas) (6)	Minor (7)	PA (8)
		Apr 01	4.2 ± 0.5	6.61 4.02 (± 0.10)	1.77	0.46	8
		Apr 30	3.8 ± 0.8	6.81 3.97 (± 0.21)	2.15	0.87	24
	8.4	Feb 28	4.6 ± 0.5	6.67 4.07 (± 0.20)	0.73	0.63	−73
		Apr 01	5.6 ± 0.4	6.70 4.11 (± 0.20)	0.92	0.52	−77
		Apr 30	5.0 ± 0.4	6.69 4.07 (± 0.20)	1.34	< 0.33	−65
	5.0	Feb 28	11.5 ± 0.7	6.85 3.79 (± 0.30)	1.50	0.72	56
		Apr 01	13.9 ± 0.9	6.83 3.74 (± 0.30)	1.85	1.07	41
		Apr 30	11.3 ± 0.7	6.88 3.88 (± 0.30)	1.82	< 0.35	30
C3	8.4	Apr 01	1.8 ± 0.4	4.45 1.87 (± 0.27)	2.71	< 0.46	19
		Apr 30	2.7 ± 0.4	4.41 2.13 (± 0.20)	2.68	< 0.41	9
D1	15.4	Jan 04	74.4 ± 3.8	−0.35 −0.12 (± 0.10)	0.14	···	···
		Jan 22	83.9 ± 4.3	−0.33 −0.14 (± 0.10)	< 0.10	···	···
		Feb 28	100.3 ± 5.2	−0.29 −0.13 (± 0.10)	0.11	···	···
		Apr 01	151.7 ± 7.6	−0.25 −0.12 (± 0.10)	0.15	···	···
		Apr 30	151.8 ± 7.6	−0.24 −0.11 (± 0.10)	< 0.10	···	···
	8.4	Feb 28	73.0 ± 3.7	−0.54 −0.24 (± 0.20)	< 0.07	···	···
		Apr 01	121.7 ± 6.1	−0.41 −0.19 (± 0.20)	0.17	···	···
		Apr 30	103.8 ± 5.2	−0.44 −0.20 (± 0.20)	< 0.05	···	···
D2	15.4	Jan 04	45.8 ± 2.4	−0.73 −0.38 (± 0.10)	0.36	···	···
		Jan 22	43.6 ± 2.4	−0.68 −0.35 (± 0.10)	0.24	···	···
		Feb 28	40.1 ± 2.4	−0.66 −0.36 (± 0.10)	0.21	···	···
		Apr 01	38.9 ± 2.1	−0.65 −0.32 (± 0.10)	0.22	···	···
		Apr 30	46.6 ± 2.5	−0.64 −0.33 (± 0.10)	0.47	···	···
	5.0	Feb 28	67.2 ± 3.4	−0.67 −0.30 (± 0.30)	< 0.18	···	···
		Apr 01	63.8 ± 3.2	−0.67 −0.32 (± 0.30)	< 0.15	···	···
		Apr 30	58.1 ± 2.9	−0.68 −0.30 (± 0.30)	0.44	···	···
E1	15.4	Jan 04	9.0 ± 0.8	−1.48 −0.77 (± 0.10)	0.48	···	···
		Jan 22	13.9 ± 1.4	−2.12 −0.89 (± 0.10)	0.69	···	···
		Feb 28	9.7 ± 1.6	−1.77 −0.75 (± 0.10)	0.68	···	···
		Apr 01	13.2 ± 1.4	−1.74 −0.70 (± 0.10)	0.92	···	···
		Apr 30	10.0 ± 1.3	−1.81 −0.72 (± 0.10)	0.84	···	···
	8.4	Feb 28	17.3 ± 1.2	−1.37 −0.74 (± 0.20)	0.76	···	···
		Apr 01	10.6 ± 0.6	−1.06 −0.55 (± 0.20)	< 0.25	···	···
		Apr 30	13.9 ± 0.9	−1.04 −0.58 (± 0.20)	0.56	···	···
E2	15.4	Jan 04	13.0 ± 1.2	−2.51 −1.02 (± 0.10)	0.82	···	···
		Jan 22	7.3 ± 1.0	−2.83 −1.26 (± 0.10)	0.50	···	···
		Feb 28	12.7 ± 1.6	−2.65 −1.21 (± 0.10)	0.73	···	···
		Apr 01	11.3 ± 1.1	−2.68 −1.27 (± 0.10)	0.58	···	···
		Apr 30	12.7 ± 1.2	−2.65 −1.18 (± 0.10)	0.75	···	···
	8.4	Feb 28	20.4 ± 1.4	−2.50 −1.07 (± 0.20)	0.87	···	···

Table 3—Continued

Component (1)	Band (2)	Epoch (3)	Flux Density (4)	$\Delta\alpha, \Delta\delta, (\sigma_p)$ (5)	Major(mas) (6)	Minor (7)	PA (8)
		Apr 01	26.6 ± 1.5	−2.32 −1.01 (± 0.20)	1.06	···	···
		Apr 30	24.9 ± 1.4	−2.39 −1.01 (± 0.20)	1.10	···	···
	5.0	Feb 28	30.1 ± 1.6	−2.20 −0.96 (± 0.30)	0.86	···	···
		Apr 01	30.0 ± 1.5	−2.20 −1.04 (± 0.30)	0.83	···	···
		Apr 30	31.7 ± 1.6	−2.24 −0.97 (± 0.30)	1.05	···	···
F1	15.4	Jan 04	6.2 ± 0.8	−4.03 −1.41 (± 0.10)	0.63	···	···
		Jan 22	4.4 ± 0.6	−4.06 −1.43 (± 0.10)	0.47	···	···
		Feb 28	6.2 ± 0.8	−3.98 −1.46 (± 0.10)	0.78	···	···
		Apr 01	6.7 ± 0.5	−4.04 −1.43 (± 0.10)	0.60	···	···
		Apr 30	4.3 ± 0.4	−4.00 −1.57 (± 0.10)	0.57	···	···
	8.4	Feb 28	10.0 ± 0.9	−3.94 −1.51 (± 0.20)	0.90	···	···
		Apr 01	10.9 ± 0.8	−3.98 −1.48 (± 0.20)	0.90	···	···
		Apr 30	8.9 ± 0.6	−3.95 −1.50 (± 0.20)	0.58	···	···
	5.0	Feb 28	17.4 ± 1.0	−3.66 −1.46 (± 0.30)	1.06	···	···
		Apr 01	19.1 ± 1.0	−3.74 −1.46 (± 0.30)	0.97	···	···
		Apr 30	16.4 ± 0.8	−3.80 −1.45 (± 0.30)	1.04	···	···
F2	15.4	Jan 04	2.4 ± 0.5	−4.52 −2.31 (± 0.10)	< 0.23	···	···
		Jan 22	1.9 ± 0.6	−4.70 −2.01 (± 0.10)	0.39	···	···
		Feb 28	1.6 ± 0.4	−4.53 −2.18 (± 0.10)	< 0.19	···	···
		Apr 01	1.5 ± 0.3	−4.77 −2.30 (± 0.10)	0.30	···	···
		Apr 30	1.5 ± 0.2	−4.73 −1.86 (± 0.10)	< 0.20	···	···
G	15.4	Jan 04	12.6 ± 1.7	−6.97 −2.65 (± 0.16)	2.47	1.27	75
		Jan 22	9.8 ± 1.6	−6.81 −2.57 (± 0.11)	1.52	1.32	−29
		Feb 28	12.4 ± 1.9	−6.66 −2.46 (± 0.18)	2.46	1.60	84
		Apr 01	14.3 ± 1.9	−6.89 −2.51 (± 0.18)	2.89	1.40	66
		Apr 30	13.1 ± 2.2	−6.89 −2.55 (± 0.23)	2.97	1.55	87
	8.4	Feb 28	26.5 ± 1.8	−6.86 −2.56 (± 0.20)	3.18	1.78	69
		Apr 01	25.7 ± 1.5	−6.86 −2.63 (± 0.20)	2.75	1.64	75
		Apr 30	26.1 ± 1.7	−6.64 −2.67 (± 0.20)	2.83	1.68	63
	5.0	Feb 28	35.8 ± 1.9	−6.80 −2.61 (± 0.30)	3.31	1.13	70
		Apr 01	36.6 ± 1.9	−6.91 −2.56 (± 0.30)	3.11	1.15	65
		Apr 30	34.6 ± 1.8	−6.84 −2.60 (± 0.30)	3.08	< 0.43	65
H	8.4	Apr 01	2.8 ± 0.4	−11.23 −4.41 (± 0.20)	2.26	0.96	46
		Apr 30	4.3 ± 1.0	−11.81 −5.16 (± 0.69)	6.20	< 1.28	59
	5.0	Feb 28	9.0 ± 1.3	−11.29 −5.18 (± 0.42)	6.17	3.03	50
		Apr 01	8.6 ± 0.9	−11.57 −5.44 (± 0.30)	5.33	2.75	48
		Apr 30	9.5 ± 1.0	−11.37 −5.10 (± 0.32)	6.88	2.96	42

Note. — Col. (1): Component label. Col. (2): Frequency (GHz). Col. (3): Epoch in 2001. Col. (4): Integrated component flux density and error (mJy). Col. (5): Offset from core ('K') component and error (mas). Col. (6): Major axis of fitted component (mas). Col. (7): Axial ratio. Col. (8): Position angle (degrees). Components: core: K; eastern jet: A1, A2, B, C1, C2, C3; western jet: D1, D2, E1, E2, F1, F2, G, H.

Table 4. Component speeds (mas/year) – slope of fitted line.

Component	Speed (mas/year)	K04 Name	K04 Speed	K04 v/c
E1	0.00 ± 0.38			
E2	0.21 ± 0.38	B	0.25 ± 0.08	3.9 ± 1.2
F1	0.04 ± 0.38	C	0.37 ± 0.15	5.8 ± 2.4
F2	0.24 ± 0.38			
G	-0.23 ± 0.68	F	0.45 ± 0.15	7.1 ± 2.4

Note. — Col. (2) gives the result of the linear fits to the data shown in Figure 4. Cols. (3), (4), and (5) show the parameters for these components in K04: component name, angular speed, and apparent velocity (v/c). We note that our apparent speeds are in agreement with those of K04 within the quoted errors.

Table 5. Fits for core shift versus frequency.

Component	Slope (mas/GHz)
E2	0.046 ± 0.014
F1	0.016 ± 0.014
G	-0.006 ± 0.018

Note. — Model results from Feb 28, Apr 01, and Apr 30, 2001, are used together for this fit.

Table 6. Helical Jet Model Parameters.

Parameter	Value	Description
θ	$6.8\,\mathrm{deg}$	inclination to line of sight
β	$0.850c$	component launch speed
ψ	$0.2\,\mathrm{deg}$	opening half-angle
ω_0	$-19.0\,\mathrm{deg}\,/yr$	angular velocity
r_0	$0.7 l.y.$	initial radius